

Chapter 3

Development of Novel TrARPES with Tunable Probe Photon Energy for 3D Quantum Materials

3.1 Research Motivation

Revealing the ultrafast dynamics of quantum materials can provide critical information into the non-equilibrium state and possible light-induced emerging phenomena [1]. Time- and angle-resolved photoemission spectroscopy (TrARPES) [2, 3] has been a powerful technique for capturing the ultrafast carrier dynamics and photo-induced phase transitions with energy-, momentum- and time-resolution. In the past decades, major progress has been made in TrARPES instrumentation, including extending the pump wavelength to mid-infrared [4] or terahertz [5], improving the energy resolution or time resolution [6–9], etc. Developments in the probe source using high harmonic generation (HHG) [10–12], or free electron laser [13] with a higher probe photon energy has also been achieved. While the power of TrARPES has been demonstrated in various quasi-two-dimensional materials such as high-temperature superconductors, topological insulators and graphene [1–3] to extract the ultrafast dynamics, so far, TrARPES studies of 3D materials such as 3D Dirac or Weyl semimetals, where intriguing light-induced dynamics and phase transitions have been predicted [14–17], have been restricted. The challenge for TrARPES measurements of these 3D materials [18] is that the Dirac or Weyl nodes exist only in isolated out-of-plane momentum (k_z) points, and highly tunable photon energy is required to access the dispersions of interests at different k_z with high precision.

The probe beam in TrARPES systems is typically generated by fourth harmonic generation (FHG) using nonlinear optical crystals β -BaB₂O₄ (BBO) with a cut-off photon energy of 6.3 eV [6]. Nonlinear optical crystal KB₂BO₃F₂ (KBBF) crystal with prism-coupled technique (KBBF-PCT) can be used to generate high-brightness table-top vacuum ultraviolet (VUV) light source [19–24] up to 7.0 eV with excellent performance for ARPES measurements [25–29]. A continuously tunable probe photon energy of 5.9–7.0 eV has been demonstrated in static ARPES measurements [27]. KBBF-based TrARPES measurements have been performed at a fixed photon

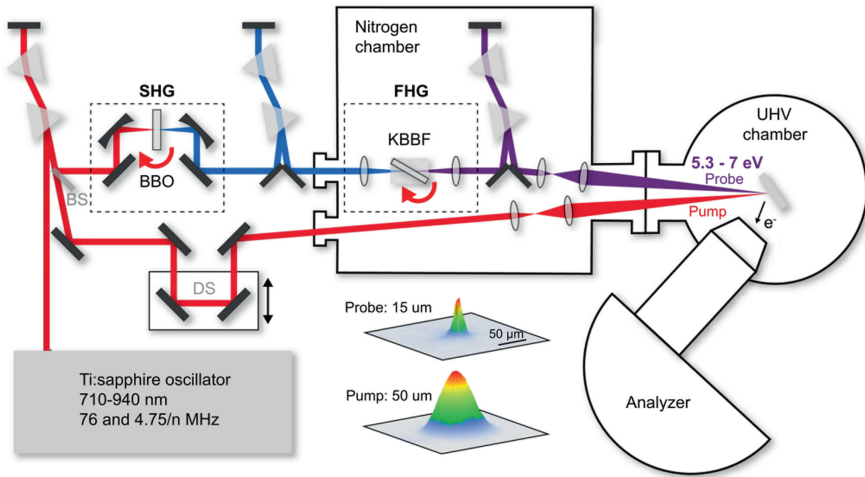


Fig. 3.1 A schematic layout of TrARPES system with tunable vacuum ultraviolet laser. BS: beam splitter, DS: delay stage, UHV: ultra-high vacuum. Transverse intensity profiles of pump and probe beams. The beam sizes are defined by full width at half maximum (FWHM). Reproduced, with permission from [31]

energy with a time resolution of ~ 1 ps [30]. Implementing TrARPES with a highly tunable probe wavelength while achieving a high time resolution is critical for further extending the ultrafast dynamics studies to 3D materials.

3.2 TrARPES with Tunable Probe Photon Energy

3.2.1 Experimental Setup

Figures 3.1 and 3.2 shows an overview of the TrARPES system. The fundamental beam (FB) with a wavelength of 710–940 nm is generated by a Ti: sapphire oscillator (Coherent Mira HP) with an output power of 2–4 W and a repetition rate of 76 MHz. The repetition rate can be reduced to 4.75/n (n is an integer) MHz by an external pulse picker. Such flexibility allows choosing an optimum repetition rate with high data acquisition efficiency while avoiding sample damage problems induced by average heating. The laser beam is firstly compressed by a prism pair compressor to compensate for the chirp from the laser cavity. A beam splitter splits the FB into two branches: 50% for the pump beam, and the other 50% is used to generate the probe beam through FHG. Compared to an amplifier which gives larger pulse energy, here a higher fraction of the FB is needed to generate the high-brightness probe beam for high measurement efficiency.

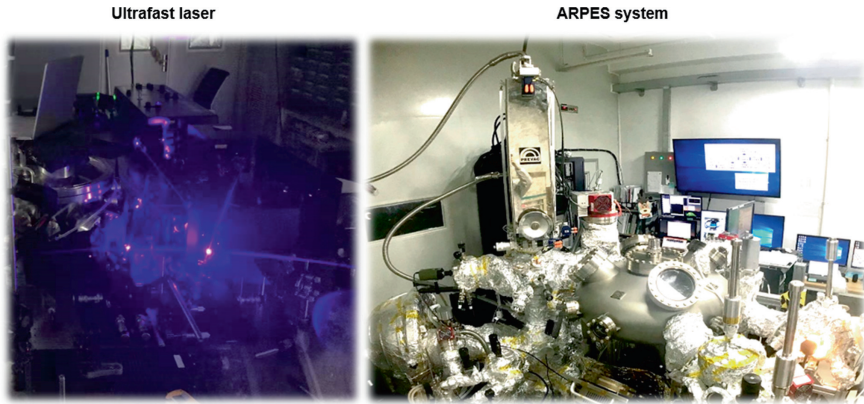


Fig. 3.2 Photographs of the TrARPES system with tunable probe photon energy

The pump beam goes through a delay stage which is used to change the delay time between the pump and probe pulses. Several silver mirrors are used to steer the beam onto the sample in the ultra-high vacuum (UHV) chamber for photoexcitation. Before entering the UHV chamber, the pump beam is focused by a lens pair with a focal length of $f = 50$ and 200 mm to obtain a beam size of $50 \mu\text{m}$ as shown in Fig. 3.1. A maximum pump fluence of $1 \text{ mJ}/\text{cm}^2$ can be applied on the sample surface.

The other 50% of the FB is used to generate the probe beam. It is first focused onto a second harmonic generation (SHG) BBO crystal with type I phase matching ($\theta = 29.2^\circ$, thickness 0.5 mm) by an off-axis parabolic mirror (aluminum coating, $f = 50 \text{ mm}$). The choice of an off-axis parabolic mirror instead of a lens is to reduce the possible chirp. The output laser beam is then collimated by another off-axis parabolic mirror and sent to a prism pair compressor to achieve optimum pulse duration for the second harmonic (SH) beam at the KBBF crystal. We would like to point out that compared to the BBO-base FHG where the FHG is achieved by passing the SH through the BBO crystal directly without generating significant chirp, compression of SH is not so critical, while in the current setup, the SH passes through a large-size prism made of fused silica with a length of 15 mm before the KBBF crystal, and the chirp is significant. For example, a 50 fs SH pulse at 400 nm is elongated to 95 fs after passing through the prism. Therefore, pre-compensation for the chirp is required to achieve the optimal pulse duration for the fourth harmonic (FH) laser. The fundamental and second harmonics lasers are separated by the first prism in the compressor, where the residual fundamental laser beam is dumped.

The SH laser beam is focused by a lens (ultra-violet fused silica, $f = 50 \text{ mm}$) onto the KBBF-PCT device [22] with type I phase matching (thickness of KBBF is 1 mm) to generate the probe beam as shown in Fig. 3.2b. The SH and FH laser beams are separated by the prism behind the KBBF crystal, to dump the residual SH laser beam. The FH laser beam is subsequently collimated by a CaF_2 lens with $f = 100 \text{ mm}$ to ensure the long-distance propagation. Then it goes into a prism pair compressor for

pulse duration compression and is finally focused by a lens pair (CaF_2 , $f = 50$ and 150 mm) to obtain a probe beam size of $15 \mu\text{m}$ on the sample surface. All the FH-related components are placed inside a nitrogen-purged chamber to avoid absorption of VUV laser for photon energy above 6.7 eV by the oxygen [32], water vapor, carbon oxide, and organic molecular in the air. The photon energies of the pump and probe beams are related by $h\nu_{probe} = 4h\nu_{pump}$ and cannot be tuned independently. However, the change in the pump photon energy is much smaller (from 1.33 to 1.75 eV), and the effect on the dynamics is negligible unless there is any resonant pumping.

The sample is mounted on a motorized manipulator in an ultrahigh vacuum (UHV) chamber with a vacuum better than 5×10^{-11} Torr. The manipulator has six degrees of freedom, allowing full control of the sample position and orientation. The sample is electrically insulated from the ground and connected to a picoammeter (Keithley 6485) to monitor the photocurrent. The energy and momentum of photoelectrons are measured by an electron analyzer (Scienta, DA30-L-8000).

3.2.2 Tunable Probe Photon Energy

The tunable probe photon energy is realized by adjusting the wavelength of the FB and corresponding phase-matching angle of nonlinear BBO and KBBF crystals. To make sure the phase matching in the entire wavelength range, the BBO is installed on a large-range rotation stage to allow rotation as indicated by the red circular arrow in Fig. 3.3a, and the KBBF-PCT device is installed on a piezoelectric driven large-range rotation stage as indicated by the red arrow in Fig. 3.3b.

3.2.2.1 High-Brightness Probe Beam Covering 5.3–7.0 eV

The input FB beam before the SHG crystal is 160 – 800 mW at a wavelength of 710 – 940 nm as shown in Fig. 3.3c and the output power of the SH laser is 9 – 250 mW at a wavelength of 355 – 470 nm as shown in Fig. 3.3d. The corresponding SH efficiency is 6 – 30% . The power of final FH laser is 3 – $430 \mu\text{W}$, which corresponds to a photon flux of 4×10^{12} – $4 \times 10^{14} \text{ s}^{-1}$ at photon energy of 5.3 – 7.0 eV (235 – 177.5 nm) as shown in Fig. 3.3e, which is much higher than typical HHG light source ($< 10^{11} \text{ s}^{-1}$) [33]. Therefore, a high-brightness probe laser beam with a tunable photon energy of 5.3 – 7.0 eV is achieved for TrARPES measurements. We note that for typical BBO-based TrARPES, the highest photon energy is 6.05 eV in the $2\omega + 2\omega$ scheme or 6.3 eV in the $\omega + 3\omega$ scheme [6]. By using KBBF-PCT, we can extend it to cover the previously inaccessible probe photon energy range of 6.3 – 7.0 eV . In addition to accessing a larger range of k_z momentum, the higher photon energy also allows probing a larger energy range below the Fermi energy.

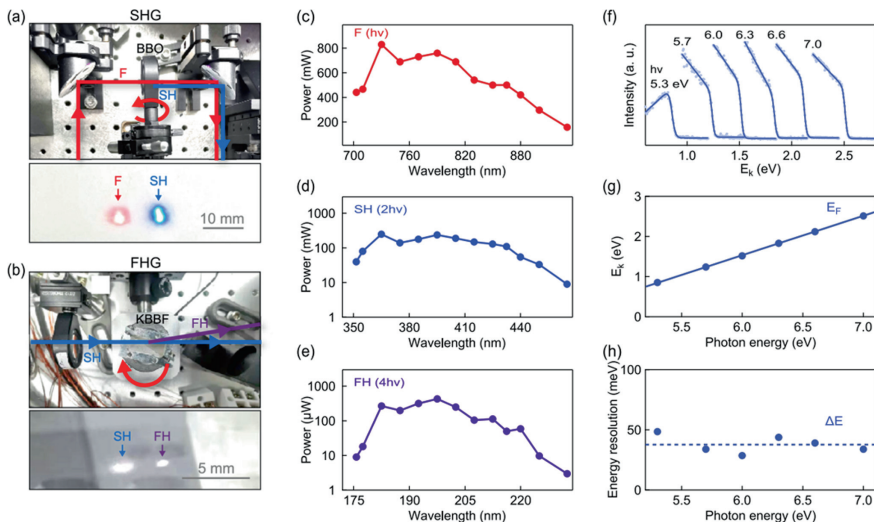


Fig. 3.3 Probe photon flux and energy resolution. **a** Photos of SHG setup and beam spots on white paper. **b** Photos of FHG setup and beam spots on the glass. **c** Fundamental laser power for SHG input as a function of fundamental wavelength. **d** Generated SH laser power as a function of SH wavelength. **e** Generated FH laser power as a function of FH wavelength. **f** Integrated EDCs on polycrystalline copper using different photon energies at 80 K. **g** Extracted kinetic energy of Fermi energy as a function of photon energy with a linear fitting. **h** Extracted energy resolution at different photon energies. The dashed line indicates the average level. Reproduced, with permission from [31]

3.2.2.2 Energy Resolutions

The energy resolution at different probe photon energies is measured on a polycrystalline copper at 80 K. The angle-integrated energy distribution curves (EDCs) for photon energies from 5.3 to 7.0 eV are shown in Fig. 3.3f. The Fermi energy (E_F) and energy resolution (ΔE) can be extracted by fitting EDCs with Fermi-Dirac function.

$$f(E) = 1/(1 + e^{\frac{E-E_F}{\Delta_{wid}/4}}), \quad (3.1)$$

where Δ_{wid} corresponds to the width of the Fermi edge and is related to ΔE by $\Delta_{wid} = \sqrt{\Delta_E^2 + \Delta_T^2}$. Here $\Delta_T = 4k_B T = 28$ meV at the measurement temperature of $T = 80$ K is induced by the thermal broadening (defined by 12–88% of the edge), which could be reduced when cooling down to a lower temperature, and ΔE is the energy resolution with contributions from the probe source, analyzer, and sample broadening. The extracted Δ_{wid} from the fitting is 40–56 meV, and the energy resolution after subtracting the contribution from the thermal broadening Δ_T is 29–48 meV for the entire photon energy range as shown in Fig. 3.3h. The energy resolution is limited by the time resolution through the uncertainty principle and could be

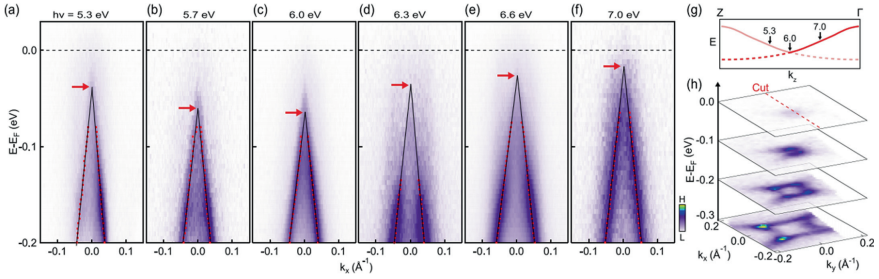


Fig. 3.4 The demonstration of the tunable photon energy on the ZrTe_5 single crystal. **a–f** Dispersion images along the direction as indicated in **h** using different photon energies. The red dots are extracted from momentum distribution curves peaks, and the black lines are the extrapolated dispersion. The red arrows indicate the top of the valence band. **g** The schematic band dispersion along k_z direction. The red curve is original dispersion and the light red curve is folded dispersion. The black arrows indicate the corresponding k_z for photon energies of 5.3, 6.0 and 7.0 eV. **h** Intensity maps at different energies using a photon energy of 7.0 eV. The measurement temperature is 80 K. Reproduced, with permission from [31]

improved by sacrificing the time resolution, for example, a higher energy resolution of 16 meV [34] can be achieved by compromising the time resolution.

3.2.2.3 Demonstrations on 3D Topological Material ZrTe_5

The suitability of such a highly tunable probe photon energy source for 3D quantum materials is demonstrated on ZrTe_5 , which is a topological material [35, 36] with strong k_z dispersion [37–40]. Figure 3.4a–f shows dispersion images measured along the Γ -X direction (indicated by the dashed line in Fig. 3.4h) at a few selected photon energies from 5.3 to 7.0 eV. This photon energy range corresponds to $k_z = 0.70 - 0.87 c^*$ [37], covering 34% of Γ -Z (half of the k_z Brillouin zone) as shown in Fig. 3.4g. For typical 3D topological materials, the lattice constant is 7.25 Å for ZrTe_5 [37], 9.7 Å for Na_3Bi [41], 12.6 Å for Cd_3As_2 [42] and 11.6 Å for TaAs [43], so the tunable photon energy of 5.3–7.0 eV can cover around 34%-60% of the half of the k_z Brillouin zone for typical 3D topological materials (assuming an inner potential of 7.5 eV [37]).

A significant change is clearly identified in the top of the valence band as indicated by red arrows in Fig. 3.4a–f, showing strong k_z dispersion. The shift of the top of the valence band toward the Fermi energy from photon energy of 6.0–7.0 eV is consistent with previous reports [40] due to the strong k_z dispersion along the Γ –Z direction as illustrated schematically in Fig. 3.4g. From 6.0 to 5.3 eV, the top of the valence band moves up, possibly due to the 1/2 reconstruction induced band folding along the k_z direction [37] as indicated by the light red curve in Fig. 3.4g.

3.2.3 Considerations for the Time Resolution

In order to capture the ultrafast electronic dynamics, a high time resolution is required. For example, typical electronic excitation or relaxation through electron-electron interaction occurs in several to tens of femtoseconds, and electron-phonon interaction occurs in hundreds of femtoseconds to several picoseconds [44, 45]. In addition, light-induced transient phenomena also emerge in a short temporal window within hundreds of femtoseconds, such as electronic oscillation induced by coherent phonon [45] and Floquet band engineering [4]. Therefore, achieving a high time resolution in TrARPES is critical for revealing electronic dynamics and light-induced exotic quantum phenomena. In the following section, the key factors for achieving high time resolution are discussed in detail.

3.2.3.1 Fourier Transform Limit

The time resolution of TrARPES is determined by the cross-correlation between pump and probe laser pulse:

$$\Delta t_{TrARPES} = \sqrt{(\Delta t_{pump})^2 + (\Delta t_{probe})^2}. \quad (3.2)$$

Therefore, the pulse durations of both pump and probe laser beams need to be optimized to reach a high time resolution.

The pulse duration is intrinsically connected to its bandwidth according to the uncertainty principle (for Gaussian pulse) [46]:

$$\Delta t \times \Delta \nu > \frac{2 \ln 2}{\pi}. \quad (3.3)$$

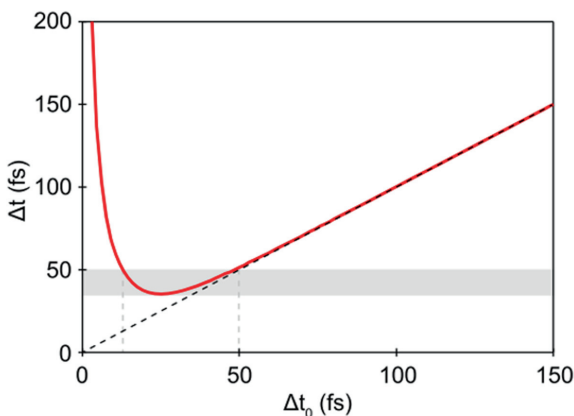
A wide enough bandwidth $\Delta \nu$ is therefore required for short laser pulses, and this sets a lower limit for the pulse duration which is Fourier-transform-limited pulse duration. For example, a pulse duration of 50 fs requires a bandwidth exceeding 20.8 nm at 820 nm.

3.2.3.2 Chirp Induced by Optical Components

The pulse duration can be elongated due to the chirp induced by the optical components, e.g. lens, crystals and windows, etc. Chirp refers to the separation of different wavelengths in the time domain after propagating through an optical component. It originates from group velocity dispersion (GVD) [47],

$$GVD = \partial(1/v_g)/\partial\omega = \partial^2 k/\partial\omega^2. \quad (3.4)$$

Fig. 3.5 Pulse duration of pump laser beam as a function of input laser pulse duration Δt_0 after adding a chirp with $GDD = 224 \text{ fs}^2$. Reproduced, with permission from [48]



When the pulse travels by a distance of l , the accumulated group delay dispersion (GDD) is

$$GDD = l \times GVD \quad (3.5)$$

and this leads to broadening of the pulse from Δt_0 (without chirp) to

$$\Delta t = \Delta t_0 \sqrt{1 + \left(\frac{4 \ln 2 \times GDD}{\Delta t_0^2} \right)^2}. \quad (3.6)$$

For example, for the pump, a beam splitter (UVFS, thickness 3 mm), a lens (UVFS, thickness 2.4 mm) before the ARPES chamber, and a window (LiF, thickness 2.5 mm) on the ARPES chamber are the main sources of chirp, which contribute an overall GDD of 224 fs^2 . Figure 3.5 shows the calculated pulse duration of the pump beam after these optical components as a function of input pulse durations Δt_0 . The calculation shows that the shortest input pulse does not necessarily lead to the best time resolution. This can be explained as follows: the shorter pulse requires a broader bandwidth which leads to a stronger chirp.

The chirp can be compensated by a prism pair (or negative GDD mirrors or gratings) which gives a negative GDD [49]:

$$GDD_{prism} = \frac{4\lambda^3}{\pi c^2} \left(- \left(\frac{dn}{d\lambda} \right)^2 L + \frac{d^2n}{d\lambda^2} D \right), \quad (3.7)$$

where L is the separation between the prisms. Two prism pairs are implemented to compensate for the chirp in the FB and FH (see Fig. 3.1).

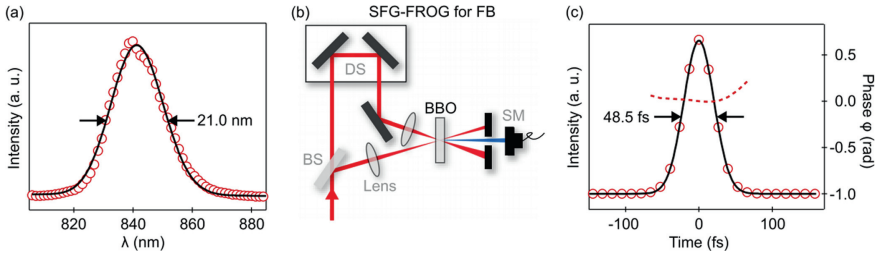


Fig. 3.6 Characterization and optimization of the FB. **a** Spectrum of the FB. **b** A schematic of the diagnosis system using SFG. The SFG signal is measured by a spectrometer. **c** Intensity and phase of FB retrieved from FROG measurement in the time domain, which gives a pulse duration of 48.5 ± 0.1 fs for the FB. Reproduced, with permission from [48]

3.2.3.3 Pulse Duration Diagnostics

In order to evaluate the effect of the compression, characterization schemes using sum-frequency generation (SFG) and difference frequency generation (DFG) have also been added to characterize the pulse duration of the FB and SH.

Here a frequency-resolved optical gating (FROG) [47] using sum-frequency generation (SFG, $\omega + \omega$ in this case) is used for the diagnostics of FB (Fig. 3.6b). The pulse intensity and phase can be retrieved by iteratively searching the signal solution $E(t, \tau)$ satisfying two constraints: $E(t, \tau) = E(t)E(t - \tau)$; $I_{FROG} = |\int_{-\infty}^{\infty} E(t, \tau) e^{-i\omega t} dt|^2$ [50]. After optimization of the compressor, the retrieved pulse in time domain shows a pulse duration of $\Delta t_F = 48.5 \pm 0.1$ fs in Fig. 3.6c. In addition, the retrieved phase (dashed curve in Fig. 3.6c) shows negligible dependence on time suggesting negligible chirp [47]. Therefore, the spectrum together with the SFG-FROG confirms that the FB satisfies the bandwidth, pulse duration and no chirp requirements.

Here we use a home-built FROG with a difference frequency generation (DFG) scheme to characterize SH as shown in Fig. 3.7a, b. The SH and FB are picked up from the main optical path by two flip mirrors and sent through an SHG BBO crystal (0.1 mm thick, thinner detection BBO than the generation BBO is required to obtain the intrinsic pulse duration) to generate a DFG signal at a frequency of $2\omega - \omega$, which is measured by a power meter. By adjusting the delay time between two beam paths, temporal information is obtained. The cross-correlation between SH and FB shows a correlation width of 66 ± 2 fs in Fig. 3.7d, implying an SH pulse duration of 46 ± 3 fs. This is also in agreement with SH bandwidth of 7.3 ± 0.1 nm (Fig. 3.7a), which corresponds a Fourier-transform-limited pulse duration of 36 fs. To further confirm that there is no chirp for the SH, the FROG-DFG image showing the wavelength-dependent DFG signal is measured by a spectrometer and shown in Fig. 3.7e. We note that a chirp pulse means a change of wavelength in the propagation of the pulse as schematically shown in Fig. 3.7g. Since the fundamental beam can be treated as a perfect reference without any chirp, the chirp of the SH can be directly

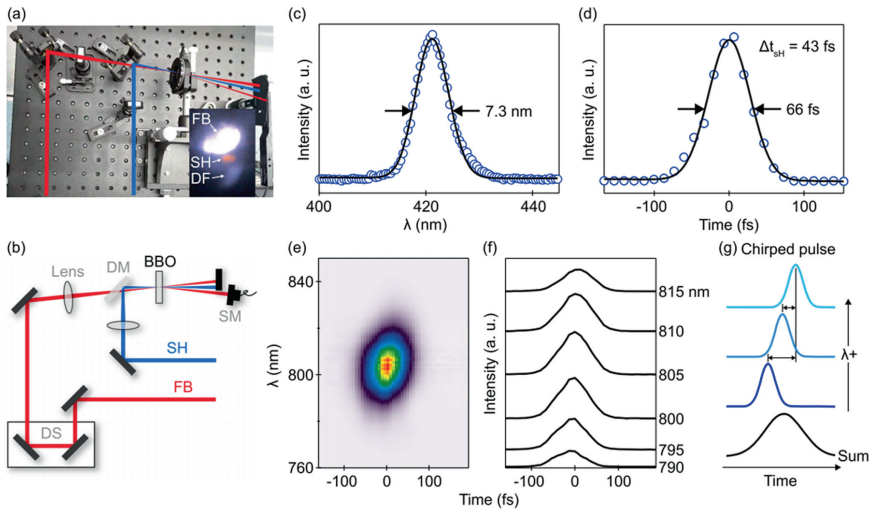


Fig. 3.7 Characterization of the SH. **a, b** Optical layout and a schematic of the SH diagnosis system. The insert shows beam spots of FB, SH, and DFG. **c** The spectrum of SH. **d** Cross-correlation from DFG between SH and FB. **e** DFG-FROG image from SH and FB. **f** Extracted time evolution curves at different wavelengths, indicating no chirp. **g** A schematic drawing of a chirped pulse in the time domain for different wavelengths. Reproduced, with permission from [48]

judged from the time shift of the cross-correlation curve at different wavelengths. The negligible time shift for different wavelengths as shown in Fig. 3.7f confirms that there is negligible chirp for the SH as expected.

3.2.3.4 Time Resolution Characterization Scheme

To evaluate the time resolution of the TrARPES setup, a reliable and efficient detection scheme is required. The time resolution can be extracted from the leading edge of the TrARPES signal, however, the leading edge is typically quite complicated due to multiple excitation channels of the photo-excited charge carriers, which are coupled to the lifetime of photo-excited carriers. Therefore, the choice of a good TrARPES sample is critical for efficient characterization and optimization of the time resolution.

We have tried polycrystalline gold, single crystal Bi_2Se_3 and molecular beam epitaxy (MBE) grown Sb_2Te_3 film on a bilayer graphene/SiC substrate. We find that the MBE grown Sb_2Te_3 film is the best for evaluating the TrARPES resolution with several advantages listed below. First of all, its TrARPES signal is much stronger than other samples, and a wide range of relaxation time scales depending on the choice of energy or momentum of the photoelectrons lead to ultra-high detection efficiency when searching for the TrARPES signal. For example, near the Fermi energy E_F , the relaxation is quite slow and photo-excited electrons above E_F persist up to 10